JOURNAL OF GEOPHYSICAL RESEARCH, VOL. 115, A07106, doi:10.1029/2009JA015099, 2010

Sun to 1 AU propagation and evolution of a slow streamer-blowout coronal mass ejection

B. J. Lynch,[1] Y. Li,[1] A. F. R. Thernisien,[2,4] E. Robbrecht,[3,4,5] G. H. Fisher,[1] J. G. Luhmann,[1] and A. Vourlidas[4]

Received 15 November 2009; revised 8 February 2010; accepted 23 March 2010; published 21 July 2010.

[1] We present a comprehensive analysis of the evolution of the classic, slow streamer-blowout CME of 1 June 2008 observed by the STEREO twin spacecraft to infer relevant properties of the pre-eruption source region which includes a substantial portion of the coronal helmet streamer belt. The CME was directed ~40° East of the Sun-Earth line and the Heliospheric Imager observations are consistent with the CME propagating essentially radially to 1 AU. The elongation-time J-map constructed from the STEREO-A HI images tracks the arrival of two density peaks that bound the magnetic flux rope ICME seen at STEREO-B on 6 June 2008. From the STEREO-A elongation-time plots we measure the ICME flux rope radial size $R_c(t)$ and find it well approximated by the constant expansion value V_{exp} = 24.5 km/s obtained from the STEREO-B declining velocity profile within the magnetic cloud. The flux rope spatial orientation, determined by forward modeling fits to the STEREO COR2 and HI1 data, approaches the observed 1 AU flux rope orientation and suggests large-scale rotation during propagation, as predicted by recent numerical simulations. We compare the ICME flux content to the PFSS model coronal field for Carrington Rotation 2070 and find sufficient streamer belt flux to account for the observed ICME poloidal/twist flux if reconnection during CME initiation process is responsible for the conversion of overlying field into the flux rope twist component in the standard fashion. However, the PFSS model field cannot account for the ICME toroidal/axial flux component. We estimate the field strength of the pre-eruption sheared/axial component in the low corona and the timescales required to accumulate this energized pre-eruption configuration via differential rotation and flux cancelation by supergranular diffusion at the polarity inversion line. We show that both mechanisms are capable of generating the desired shear component over time periods of roughly 1–2 months. We discuss the implications for slow streamer-blowout CMEs arising as a natural consequence of the corona's re-adjustment to the long term evolutionary driving of the photospheric fields.

Citation: Lynch, B. J., Y. Li, A. F. R. Thernisien, E. Robbrecht, G. H. Fisher, J. G. Luhmann, and A. Vourlidas (2010), Sun to 1 AU propagation and evolution of a slow streamer-blowout coronal mass ejection, *J. Geophys. Res.*, *115*, A07106, doi:10.1029/2009JA015099.

1. Introduction and Event Overview

[2] The twin spacecraft of the STEREO mission were separated by ~55° during the first week of June 2008. This separation is large enough to be considered the beginning of "quadrature" viewing geometry, where certain limb CME events seen by one of the spacecraft could be headed directly toward the other. Thus, remote sensing observations of unprecedented quality can be combined with in situ particle and field measurements for the same CME event, including for the first time, with continuous observational coverage of the CME's propagation from the Sun to 1 AU.

[3] The STEREO-A (STA) spacecraft observed a classic streamer-blowout CME with subtle 171 Å emission signatures of an extended slow rise phase beginning at 31 May 2008 21:24 UT over the East limb in the Extreme Ultraviolet Imager (EUVI) data. The slow rise phase is also visible in the COR1 coronagraph data and we define the start of the eruption as the transition in the *Robbrecht et al.* [2009] height-time data which is coincident with the CME front becoming visible in COR2 coronagraph data on 1 June 2008 19:00 UT. This particular slow CME had virtually

[1]Space Sciences Laboratory, University of California, Berkeley, California, USA.
[2]University Space Research Association, Columbia, Maryland, USA.
[3]George Mason University, Fairfax, Virginia, USA.
[4]Space Sciences Division, Naval Research Laboratory, Washington, D.C., USA.
[5]Now at Department of Space Physics, Royal Observatory of Belgium, Brussels, Belgium.

0148-0227/10/2009JA015099

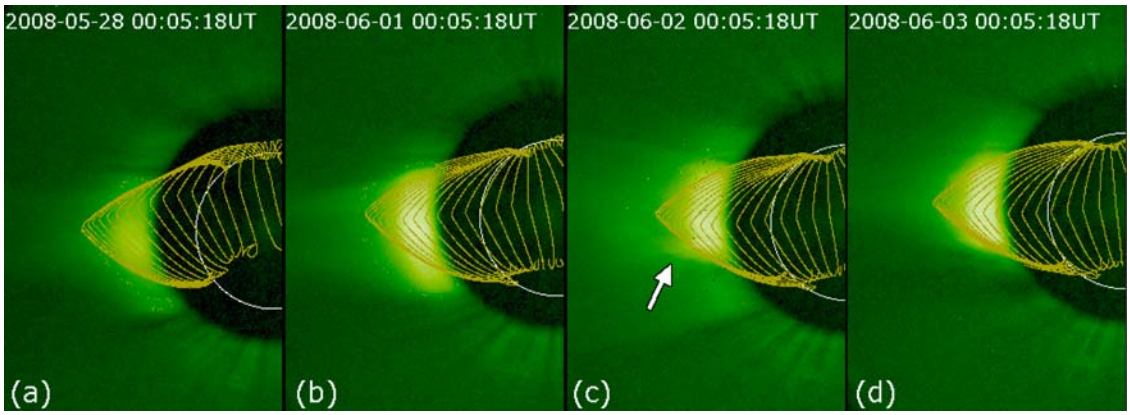

Figure 1. The streamer blowout CME began on 1 June 2008 observed by STEREO-A. SECCHI COR1-A images are overlaid with the PFSS streamer arcade based on the polar-corrected MDI synoptic map for CR2070. (a and b)The East limb streamer was "swollen" several days before the CME. (c) The CME is visible as a faint cavity with brighter core material showing the flux rope pinch-off (indicated by arrow). (d) The post-CME COR1 white light emission is in better agreement with the PFSS streamer belt arcades, suggesting the lower portion of the pre-CME streamer was in an energized non-potential state.

none of the usual CME or post-CME coronal EUV signatures [see *Robbrecht et al.*, 2009], however the CME disturbance was observed throughout the STA COR1, COR2, HI1, and HI2 instruments of the SECCHI suite [*Howard et al.*, 2008] and in situ as a classic magnetic cloud ICME from 6 June 2008 22:00 UT to 7 June 2008 14:20 UT by the STEREO-B (STB) IMPACT [*Luhmann et al.*, 2008] and PLASTIC [*Galvin et al.*, 2008] instruments. The low-coronal evolution of this event was extensively described by *Robbrecht et al.* [2009], and we summarize as follows. The event evolved very slowly and is typical of the streamer-blowout class of CMEs [*Vourlidas et al.*, 2002]. The COR2-A coronagraph observed a slow flux rope type CME, while an extremely faint partial halo was observed in COR2-B. The CME propagation direction was found to be ~40° East of Sun-Earth line using images from the stereoscopic views [*Robbrecht et al.*, 2009; *Thernisien et al.*, 2009], and therefore, the CME was expected to have a front-side source visible in both the STB and Earth view of the solar disk. The peculiarity of this event was precisely the lack of any clear eruption signature(s) in EUVI-B images or any obvious magnetic source region in the SOHO MDI magnetograms. The lack of the usual disk CME signatures was interpreted as being due to some combination of weak magnetic fields and the large initiation height of the CME. The EUVI-A 171 Å images however, did show a concave feature above the East limb that rose very slowly and developed into the CME core. This event clearly demonstrates that large CMEs may have disk-signatures that are weak or even undetectable.

[4] *Möstl et al.* [2009] presented a concise summary of the relationship between aspects of the remote sensing CME signatures and the in situ ICME signatures at 1 AU. These authors linked the traditional 3-part CME white-light intensity structure to in situ density enhancements surrounding the coherent ICME field structure and argued the specific arc shape of the intensity fronts in the HI images could be related to the in situ flux rope orientation. Analyzing the ICME field structure with two popular flux rope models, *Möstl et al.* [2009] conclude that flux content of this event implies the existence of a pre-eruption coronal flux rope. In this paper we will argue the opposite scenario by using the detailed evolution of the interplanetary flux rope to estimate the magnitude of the coronal sheared field component that would evolve into the ICME axial/toroidal flux during the CME eruption. We examine the feasibility of building up this amount of shear through the standard, large-scale processes of photospheric field evolution and conclude there is no need to invoke a pre-existing highly twisted coronal flux rope.

[5] Figure 1 shows the temporal evolution of the East limb streamer in COR1-A leading up to, during, and after the streamer blowout CME. Also plotted in each panel are representative magnetic field lines showing the boundary of the helmet streamer belt computed from the Potential Field Source Surface (PFSS) model [e.g., *Wang and Sheeley*, 1992; *Luhmann et al.*, 1998]. The PFSS modeling used the SOHO/MDI [*Scherrer et al.*, 1995] polar-corrected synoptic map data [*Liu et al.*, 2007] for Carrington Rotation (CR) 2070 and $l_{max} = 36$ in the spherical harmonic expansion. The potential field represents the minimum energy state of the corona for a given radial magnetic field distribution on the inner boundary. The PFSS streamer orientation agrees with the COR1 scattered white light intensity except for the location of the southern boundary. Specifically, the COR1 streamer is swollen beyond the predicted PFSS streamer belt width for several days leading up the CME eruption. Figure 1c captures some of the CME lift-off and detachment from the streamer belt, visible as an intensity enhancement in an X-shape at roughly $2.5R_{\odot}$, indicated by the arrow. It is important to note that after the CME has erupted, Figure 1d shows the COR1 streamer width has decreased and is in better agreement with the PFSS streamer configuration. This implies that even in the case of this very slow streamer blowout CME, the eruption plays an important part of the process that relaxes the coronal field to a state of less accumulated magnetic stress and free energy.

[6] The structure of the paper is as follows. In section 2, we first analyze the inner heliospheric evolution of this streamer-blowout CME as observed by the STA SECCHI imaging suite and show that it is now possible to track a

relatively isolated, large solar transient continuously from the Sun to ~1 AU, where the magnetic field and plasma properties of the CME were observed in situ by STB. In section 3 we present the in situ observations by STB and describe the simple magnetic cloud model fit to the field rotation. In section 4 we describe the temporal and spatial orientation and evolution of the CME/ICME flux rope structure. Finally, in section 5, we combine aspects of the remote and in situ observations in an attempt to place some constraints on estimates of the CME source region properties, specifically, the magnetic field magnitude of the pre-eruption shear component (or axial flux rope fields) and the flux content of a section of the helmet streamer belt. We conclude with a brief discussion of the impact or contribution that such "sourceless" CMEs might have during various phases of the solar cycle.

2. CME/ICME Tracking in STEREO-A COR2, HI1 and HI2

2.1. Measuring Elongation Angle Versus Time

[7] One of the most useful tools for tracking the heliospheric evolution of white light intensity features through the HI fields of view is the technique of constructing elongation-time plots from running-difference images [e.g., *Harrison et al.*, 2009, and references therein]. The elongation angle of an intensity feature in the Heliospheric Imager data is the angular distance from the feature to the Sun's center relative to the observing spacecraft. The elongation-time plots are the STEREO version of the height-time analysis developed and refined with the high quality, high cadence SOHO LASCO data [see *Sheeley et al.*, 1999].

[8] SECCHI elongation-time plots have already been used to characterize the solar wind's Parker spiral shape [*Sheeley et al.*, 2008a], identify recurrent stream structure and CIRs [*Sheeley et al.*, 2008b], and follow the heliospheric evolution of CME transients [*Davies et al.*, 2009; *Davis et al.*, 2009; *Harrison et al.*, 2008, 2010; *Rouillard et al.*, 2009; *Webb et al.*, 2009; *Möstl et al.*, 2009].

[9] Figure 2 plots several frames of the STA SECCHI running-difference data showing the evolution and propagation of the CME. Figures 2a and 2b are COR2 running difference images showing the classic highly-structured, 3-part flux rope CME signatures in a $15R_\odot \times 15R_\odot$ region of the COR2 field of view (FOV). Here, we have also labeled various quantities that will be useful in the analysis in the following sections; for the CME in COR2 we show the radial flux rope diameter Δr and the CME's angular width W. Figures 2c and 2d show the CME evolution in HI1 running difference data in the 20° × 20° FOV. The equivalent geometrical quantities are the CME elongation angular extent $\Delta\alpha$ and the elevation angles δ_1, δ_2 associated with the CME's angular extent above and below the ecliptic plane. Figures 2e and 2f show the CME's running difference signal in the HI2 70° × 70° FOV. We only indicate $\Delta\alpha$ in the HI2 images because the signal strength rapidly decreases for larger elevation angles.

[10] Figure 3 plots the combined elongation-time plot at the position angle of PA = 96° (roughly the $\delta = 0°$ lines in Figure 2) for the STA COR2, HI1, and HI2 data. The average position of STB for our time period of interest, 1 June 2008 through 7 June 2008 is located at 67.75° elongation angle in STA HI2's FOV. Here we have truncated the elongation-time plot at STB's position and plotted in the top panel the in situ time series of solar wind proton density N_p observed by STB IMPACT. The two main elongation-time track features represent the leading edge compression density enhancement in front of the CME and the trailing edge core density enhancement are indicated with the two arrows. These tracks line up with and obviously correspond to the large in situ density spikes in the STB data and define the boundaries of the magnetic cloud signatures in the STB magnetic field and plasma data. With these near-quadrature STEREO observations *Möstl et al.* [2009] were able to directly associate white-light structures in CME images with the ICME field and plasma properties observed in situ.

[11] In order to unravel a meaningful distance from the line-of-sight (LOS) integrated HI signal, we require, for limb or quadrature events, an assumption of the "true" propagation direction. For Earth-directed events, one can use the three viewpoints provided by STA, STB, and SOHO at L1 to pinpoint the propagation direction through geometric triangulation and other reconstruction techniques [e.g., *Mierla et al.*, 2009; *Temmer et al.*, 2009; *Liu et al.*, 2009].

2.2. Estimating Distance From HI Angular Separation

[12] Figure 4 (left) plots the observing geometry for the CME/ICME propagation and labels the distances, angles, and white light scattering geometric surfaces. The thick red circle surrounding STB is the size of the model cylindrical flux rope used to fit the STB in situ field rotations (section 3), whereas the red ellipse is more representative of the actual ICME azimuthal extent [e.g. section 3 and *Robbrecht et al.*, 2009]. The distance of the STA spacecraft from the Sun $r_{STA} = 0.944$ AU is taken to be the mean position over the time interval of interest. The angular extent of the HI1-A FOV is shown as the light blue lines and the HI2-A FOV is bounded by the light yellow lines. The STA plane-of-the-sky and Thomson sphere [*Vourlidas and Howard*, 2006] are plotted as dark blue lines and labeled "STA POS" and "STA TS" respectively. The following analysis for determining actual distances from observed elongation angles is modeled after that of *Sheeley et al.* [2008a, 2008b] (Here we also adopt the notation of *Sheeley et al.* [2008b], where the elongation angle is denoted by α. The elongation angle α should not be confused with the equation (4) field-aligned current density coefficient for force-free magnetic fields.). Using the law of sines and the $\sin(\pi - x) = \sin(x)$ identity, we obtain

$$r_0 = r_{STA}\frac{\sin\alpha_0}{\sin(\lambda+\alpha_0)}, \tag{1}$$

where λ is the angle between STA and the CME propagation direction. The elongation angle of the electron density at the location $\boldsymbol{r}_0$ is defined as α_0. Likewise, the point $\boldsymbol{r}_1 = \boldsymbol{r}_0 + \Delta\boldsymbol{r}$ can be expressed in terms of an angular width $\Delta\alpha$ and r_0,

$$r_0 + \Delta r = r_{STA}\frac{\sin(\alpha_0+\Delta\alpha)}{\sin(\lambda+\alpha_0+\Delta\alpha)}. \tag{2}$$

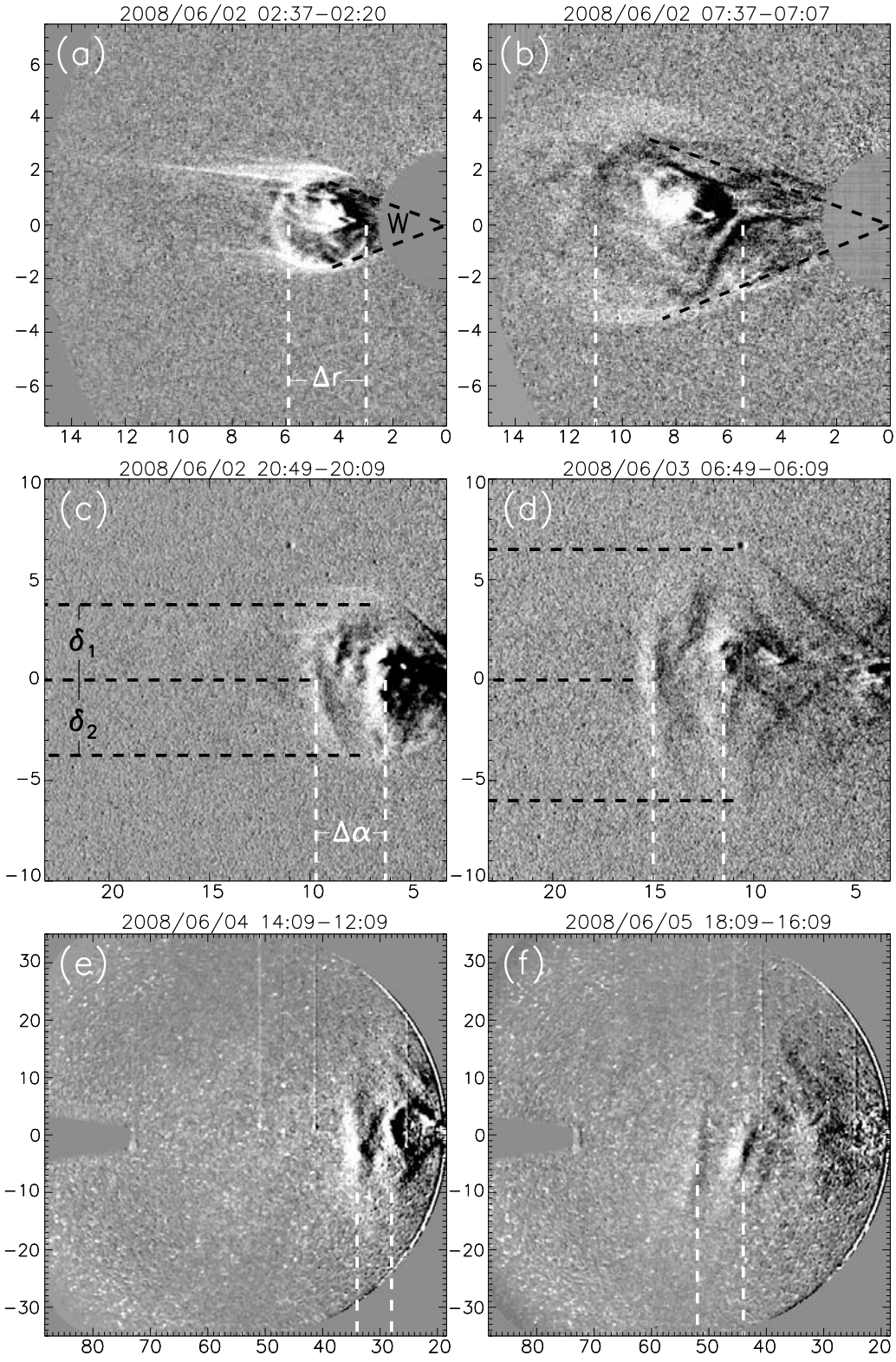

Figure 2. Running difference images from STEREO-A SECCHI data in COR2 (a and b), HI1 (c and d), and HI2 (e and f). The axis units are in $R_\odot$ for the COR2 data and elongation, elevation angle in the HI data. Geometric quantities used in the analysis include the radial CME distance Δr and the angular width W in COR2, the elongation angular width $\Delta\alpha$ in HI1 and HI2, and the maximum/minimum elevation angles δ_1, δ_2 in HI1. See text for additional details.

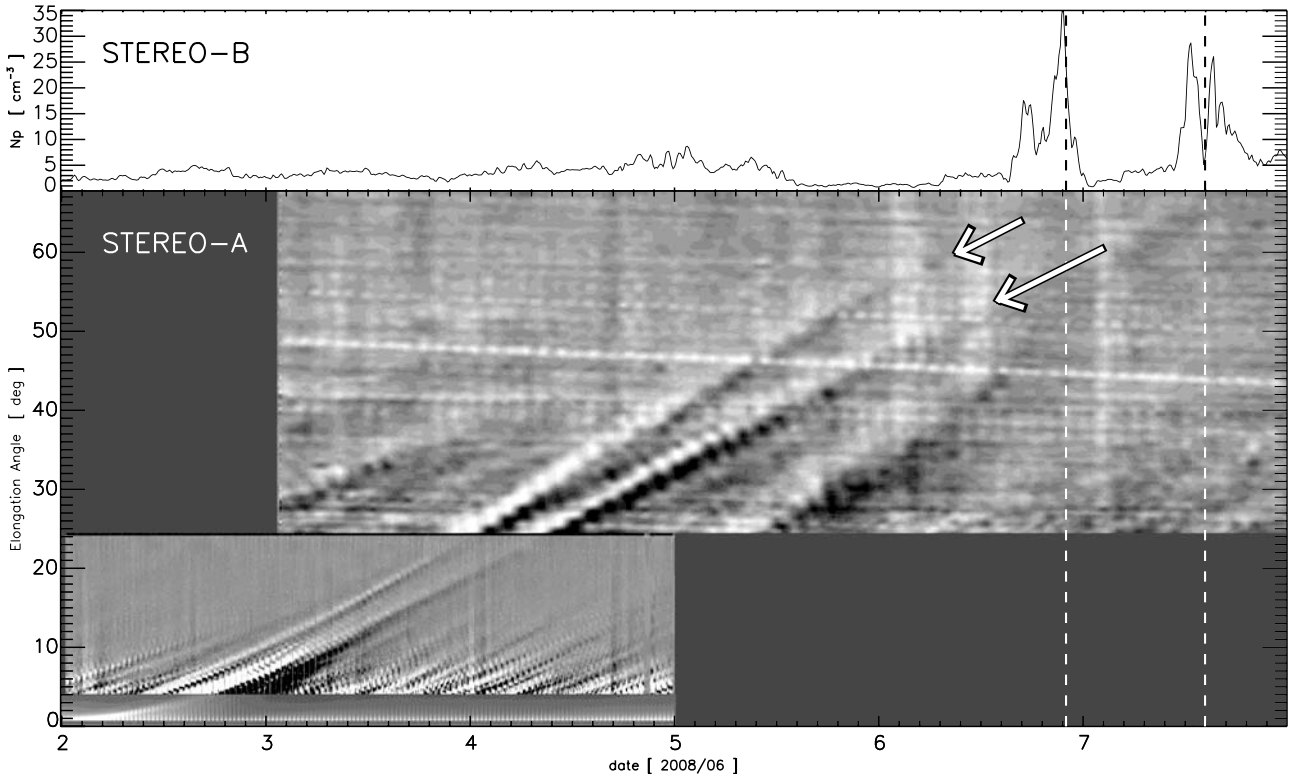

Figure 3. (top) The time series of STEREO-B proton number density for the 2 June 2008 through 7 June 2008 time period. (bottom) The elongation-time J-map from the combined STEREO-A COR2 base difference and HI1, HI2 running difference images. The vertical dotted lines indicate the boundaries of the magnetic cloud flux rope signature in the STB magnetic field data and appears to coincide almost exactly with the region bounded by the leading and trailing elongation-time tracks in the STA data. The arrows point to the main tracks measured in Figure 4.

The apparent location of the line-of-sight integrated intensity signal is the intersection of the LOS with the TS (the point of maximum scattering emission), shown as the black asterisks on the blue circle in the Figure 4 (left).

[13] Figure 4 (right) plots the observed STA HI1, HI2 elongation-time data (squares, triangles) of the leading edge and core/trailing edge features shown in Figure 3 (corresponding to the dashed lines in Figure 2), as well as the analytical curves for α_0 and $\alpha_0 + \Delta\alpha$ for two specific CME propagation directions approximately 10° either side of the *Robbrecht et al.* [2009] value: $\lambda = 74.5°$ is plotted in green and $\lambda = 55.1°$, plotted in blue, is the propagation direction directly toward STB. *Möstl et al.* [2009] compared a number of techniques to determine the heliospheric propagation direction (see their Table 1) and found that they all gave results consistent with this $\lambda \sim 55$–$75°$ range.

[14] *Sheeley et al.* [2008b] show, assuming constant radial speed, the formula for the elongation angle as a function of time is

$$\alpha(t) = \arctan\left(\frac{x(t)\sin\lambda}{1 - x(t)\cos\lambda}\right), \tag{3}$$

with $x(t)$ being the normalized radial distance. Our normalized distances take the form $x(t) = (\langle V_r\rangle \pm V_{\exp})t/r_{\mathrm{STA}}$ where we set $\langle V_r\rangle = 390$ km/s, the average in situ radial velocity at STB (see section 4.1). Here, $\alpha_0(t)$ corresponding to the trailing intensity enhancement with a radial speed $\langle V_r\rangle - V_{\exp}$ and the leading edge intensity enhancement is $\alpha_0(t) + \Delta\alpha(t)$ corresponding to $\langle V_r\rangle + V_{\exp}$. From the *Robbrecht et al.* [2009] height-time analysis through the COR2-A FOV we note that it takes ~24 hours for the CME feature tracked to obtain the average STB in situ radial velocity $\langle V_r\rangle$ with a linear temporal dependence. Therefore, to travel the fixed radial distance of the first HI1-A data points, we must offset the theoretical elongation-time curves by 12 hours. It is clear from Figures 2 and 4 that the radial extent of the ICME can be considered the diameter of the flux rope structure, i.e. $\Delta r(t) = 2R_c(t)$. The propagation direction and radial evolution will factor into analysis and interpretation of the ICME flux rope properties in section 4.

3. In Situ Observations by STEREO-B

[15] Figure 5 plots the 10 minute average STB magnetic field and plasma data obtained from the IMPACT and PLASTIC instruments for the period of 5 June 2008 22:40 UT through 8 June 2008 17:20 UT in time units of hours since 2 June 2008 00:00 UT. Starting from the top panel and moving down the plot, we show the bulk radial velocity, proton density, proton temperature, plasma beta (The IMPACT data is available on the UCLA STEREO page http://dawn.ucla.edu/ssc/stereo/ and the plasma β is calculated according to the formula $\beta = 10^{-5}N_p(469895.8 +$

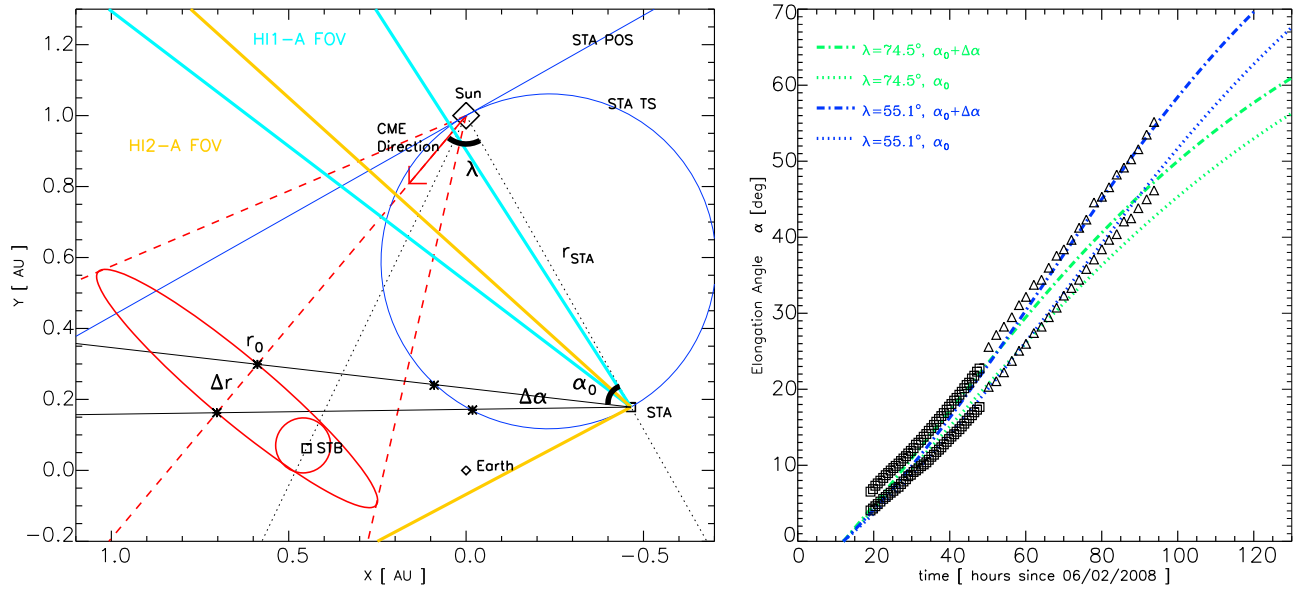

Figure 4. (Left) The STEREO observing geometry and geometric parameters for tracking the CME/ICME through the HI data. The CME propagation angle with respect to STA is shown as λ, while α_0 is the elongation angle of the LOS-integrated signal with maximum scattering intensity at the asterisk on the STA TS corresponding to the physical CME feature(s) at an estimated radial distance r_0 from the Sun. The CME's angular elongation $\Delta\alpha$ represents a CME radial extent of Δr. The circle plotted around STB is the size of the LFF cylinder used to fit the in situ magnetic field rotation of the ICME (section 3). (right) The elongation-time measurements from HI1 (squares) and HI2 (triangles) for the two prominent tracks in the Figure 3 J-map. Also plotted are the theoretical elongation-time curves for a constant 390 km/s radial velocity at λ = 74.5° (green) and 55.1° (blue) propagation directions.

4.048 T_p)/B^2 with the units of N_p in cm^{-3}, T_p in K, and B in nT (see *Jian et al.* [2006] for details)), the magnetic field vector in RTN coordinates and its magnitude. The in situ solar wind data clearly show a number of the classic field and plasma signatures that commonly describe ICMEs with large-scale, coherent internal field structure, now known as magnetic clouds (MCs). These signatures include an extended period of enhanced magnetic field magnitude, a smooth field rotation over a large angle, and low proton temperature or plasma beta [*Klein and Burlaga*, 1982]. MC ICMEs often coincide with periods of counter-streaming electrons, smooth, declining velocity profiles, and enhanced elemental and ionic composition signatures [e.g., see *Zurbuchen and Richardson*, 2006, and references therein].

[16] The boundary of the STB magnetic cloud is shown in Figure 5 by two vertical dashed lines at 6 June 2008 22:00 UT and 7 June 2008 14:20 UT. In general, there can be a significant uncertainty associated with the specific boundary selection of the magnetic cloud portion of the ICME [e.g., *Riley et al.*, 2004; *Lynch et al.*, 2005]. However, given the relatively quiet ambient solar wind conditions and that the coherent magnetic field rotations line up exactly with the sharp transition to low-β and the declining velocity profile, the boundary selection is relatively straight forward in this event.

[17] The magnetic cloud field rotation is fit with the simple linear, force-free (LFF) cylinder model [e.g., *Lundquist*, 1950; *Goldstein*, 1983; *Burlaga*, 1988] using the two step optimization method to minimize the mean square error between the data and model [after *Lepping et al.*, 1990]. The LFF cylinder model is the constant-α solution of the equation $\nabla \times \boldsymbol{B} = \alpha \boldsymbol{B}$ in cylindrical coordinates (ρ, ϕ, z). This gives

$$\boldsymbol{B}(\rho) = HB_0 J_1(\alpha\rho)\hat{\phi} + B_0 J_0(\alpha\rho)\hat{z}, \tag{4}$$

in terms of the J_0 and J_1 Bessel functions, where we choose $\alpha = x_{01}/R_c$ to be the first zero of J_0 (i.e., $x_{01} \sim 2.408$) divided by the cylinder radius R_c. The spatial orientation of the model cylinder is given by three parameters; the symmetry axis makes an angle of ϕ_0 with the Sun-to-STB radial direction, is tilted out of the ecliptic plane by θ_0, and the spacecraft passes a normalized distance ρ_0/R_c from the cylinder axis at the point of closet approach. The spatial angles are defined with respect to the RTN coordinate system are shown in Figure 6 along with a schematic of the LFF cylinder model. The best-fit spatial orientation of the cylinder model is ϕ_0 = 270.8°, θ_0 = 45.8°, and $|\rho_0/R_c|$ = 0.162, corresponding to a moderately inclined flux rope with a small spacecraft impact parameter. The MC field rotation shows right-handed chirality H = +1, and the field strength on the model cylinder axis is B_0 = 16.31 nT. The model cylinder flux rope radius is R_c = 0.0775 AU. The LFF cylinder model fit to the 3-dimensional MC field rotation is also shown in Figure 5 as the thick gray lines in the RTN field components and magnitude. The error measures for the rotation and field magnitude fits are $\chi^2_{\rm dir}$ = 0.0678 and $\chi^2_{\rm mag}$ = 4.573 respectively, which imply a "good" quality fit [*Lynch et al.*, 2003]. We note that *Möstl et al.* [2009] has independently fit this event with a similar LFF cylindrical model as well as the Grad-Shafranov reconstruction technique and obtained fitting results and physical parameters

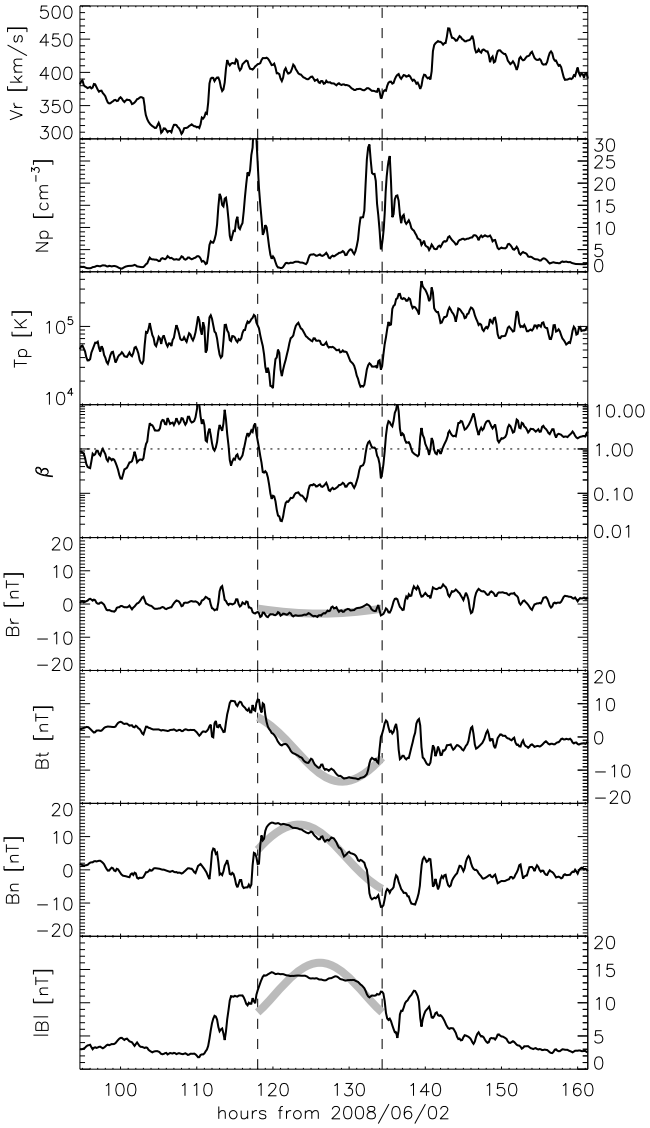

Figure 5. STEREO-B IMPACT and PLASTIC observations of the plasma and interplanetary magnetic field. From top to bottom we plot bulk radial velocity V_r, proton number density N_p, proton temperature T_p, plasma beta β, and the magnetic field in RTN coordinates and its magnitude. The vertical dashed lines indicate the magnetic cloud boundaries (corresponding to the vertical dashed lines in Figure 3) and the thick gray lines plot the LFF cylinder model magnetic field fit to the data. The fit parameters are described in section 3.

that are essentially identical (within the model uncertainties) to what we have presented here.

4. Flux Rope Structure, Orientation and Evolution

4.1. Radial Expansion

[18] Since we have continuous observations of the entire CME/ICME transit from the Sun to 1 AU, if we extrapolate back the flux rope radial size inferred by the in situ data we ought to get results consistent with the spatial distances between the elongation-time features corresponding to the flux rope boundaries. The analysis that follows is essentially the method used by *Rouillard et al.* [2009], and likewise, we obtain HI radial expansion rates that agree with the flux rope expansion estimate from the in situ observations.

[19] The in situ size of the MC, assuming a constant radial velocity of $\langle V_r \rangle = 390$ km s^{-1} for the cloud duration of $\Delta T =$ 16.33 hrs and the 3D cylinder orientation, gives a diameter of $2R_c = 0.155$ AU. The common interpretation of the declining radial velocity profile is that the flux rope is expanding and the leading and trailing MC edges have velocities given by $\langle V_r \rangle \pm V_{\rm exp}$ where $\langle V_r \rangle$ is the bulk speed at the center of the cloud. For reasonable impact parameters, the bulk and expansion speeds can be obtained via a simple linear fit to the radial velocity profile [e.g., *Farrugia et al.*, 1993; *Kumar and Rust*, 1996; *Owens et al.*, 2005]. In our case this yields, correcting for the $\rho_0 = 0.162R_c$ impact parameter, a MC cross section expansion velocity of $V_{\rm exp} =$ 24.48 km s^{-1} (the uncorrected expansion velocity from the observed radial velocity profile is 24.16 km s^{-1} so the model fit-dependent projection is quite minor). Figure 7a plots 10 minute averages of the bulk radial velocity during the MC interval used to determine $\langle V_r \rangle$ and $V_{\rm exp}$.

[20] If this MC expansion velocity is constant in time, then we can extrapolate back to a predicted (and measurable) size in the HI or COR2 fields of view. The simple constant-$V_{\rm exp}$ assumption has been shown to be quite reasonable for a number of "classic" magnetic cloud events [*Russell and Shinde*, 2003]. Figure 7b plots the flux rope radius determined from the in situ measurements at STB (large diamond) and the CME/ICME radial size estimated from the STA COR2 (asterisks), HI1 (squares), and HI2 (triangles) running difference image sequences as function of their observation time. The CME flux rope radius estimate is straight forward in the COR2 field of view because of the sky-plane assumption and the circular shape of the CME; we overplot a circle on the running difference image and convert the pixel size to a physical distance. The pixels in HI data have angular units and the sky-plane assumption breaks down for moderate-to-large elongation angles, thus requiring a proper treatment of the Thomson sphere formalism [*Vourlidas and Howard*, 2006], as described in section 2.2.

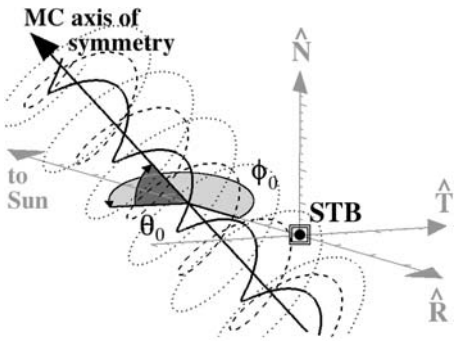

Figure 6. Schematic diagram of the RTN coordinate system centered at STEREO-B. Representative magnetic field lines from the LFF cylinder model are plotted around the cylinder axis of symmetry. The MC model spatial orientation parameters ϕ_0 and θ_0 are labeled.

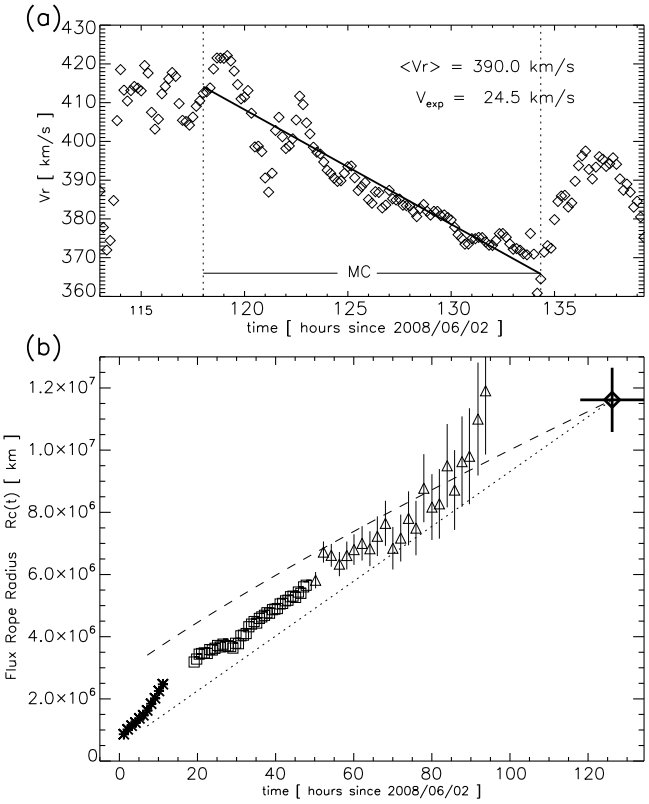

Figure 7. (a) STB bulk plasma V_r and the linear fit to find V_{exp}. (b) The inferred flux rope radius R_c = 1.16 ± 0.10 × 10^7 km at STB (diamond), the $R_c(t)$ predictions from a constant-V_{exp} (dotted line) and the *Bothmer and Schwenn* [1994] empirical scaling law (dashed line), and the measured $R_c(t)$ points from the STA running difference data from COR2 (asterisks), HI1 (squares), and HI2 (triangles). The horizontal error bars on the STB value indicate the MC event duration and the vertical error bars show the 1σ uncertainty in the LFF model R_c value. The error bars on the HI1 and HI2 points come from the two different CME propagation angles. See text for additional details.

[21] To calculate our constant-V_{exp} CME size we take the midpoint of the cloud to be the ~1 AU final time t_f at 7 June 2008 06:10 UT and obtain

$$R_c(t) = R_c(t_f) - V_{\exp}(t_f - t), \tag{5}$$

which is plotted as the dotted line in Figure 7b. This model predicts a CME radius of size zero at time t_0 = 1 June 2008 18:21 UT which clearly underestimates the actual CME size in the early stages of the eruption. Alternatively, *Bothmer and Schwenn* [1994] have derived an empirical scaling law for interplanetary MC flux rope sizes by analyzing many events observed by Helios 1/2, Pioneer 10, and Voyager 1/2 spacecraft at different heliocentric distances. They obtain a power law relationship, $2R_c(r) = \langle 2R_c \rangle_{1AU} \times (r/1\ AU)^{0.78\pm0.10}$, where the average 1 AU MC flux rope diameter is given by $\langle 2R_c \rangle_{1AU}$ = 0.24 AU. *Russell et al.* [2003] have shown that, for a couple of events observed by both the ACE and NEAR spacecraft, the radial variation of individual MC flux rope sizes are also consistent with the *Bothmer and Schwenn* [1994] scaling law. If we were to apply this scaling law to our STB MC and assume a constant radial speed corresponding to the observed $\langle V_r \rangle$ then we estimate

$$R_c(t) = R_c(t_f)\left(\frac{t}{t_f}\right)^{0.78}, \tag{6}$$

which is also plotted in Figure 7b as the dashed line. Our application of the *Bothmer and Schwenn* [1994] scaling law breaks down when the CME radial speed is no longer constant and *Robbrecht et al.* [2009] showed that the CME radial velocity was still increasing through the STA COR2 field of view. Obviously, a more complex analysis is required to describe the rapid CME expansion during its near-Sun acceleration and evolution [see, e.g. *Zhang and Dere*, 2006; *Schwenn et al.*, 2006, and references therein].

[22] However, taken together, these two methods appear to both be reasonable approximations for the expansion of the radial component of CME/ICMEs, providing a lower and upper bounds on the size of the flux rope CME. Our size estimates from the STA SECCHI data throughout the 1 AU transit consistently fall above the constant-V_{exp} scaling and below the empirical *Bothmer and Schwenn* [1994] scaling law assuming constant $\langle V_r \rangle$ until approximately t = 90 hours after 2 June 2008. The apparent, relatively fast increase of the inferred radial size towards the end of the HI2-A data is an artifact of the viewing geometry. This phenomena is a combination of two different effects that are captured in Figure 4. First, in the left panel that shows the viewing geometry schematic, notice the observational line-of-sight to point $\boldsymbol{r}_0$ intersects a portion of the ICME ellipse that is further away from the Thomson sphere than the line-of-sight to point $\boldsymbol{r}_0 + \Delta\boldsymbol{r}$. Thus, the trailing edge intensity becomes fainter and slower relative to the intensity of the leading edge, which appears to speed up as different parts of the ICME are sampled. Second, the right panel of Figure 4 shows that the time of the rapid FR radius increase $t >$ 80 hours corresponds to an HI2 elongation angle of >45°, precisely where *Vourlidas and Howard* [2006] argue that the Thomson scattering signal strength is expected to rapidly decrease and the measurement uncertainties rapidly increase. Therefore, we conclude that this particular streamer blowout flux rope CME must be fairly typical in its interplanetary radial expansion.

4.2. Forward Modeling Interplanetary Flux Rope Orientation

[23] The large-scale rotation of CME flux rope structures during their eruption and interplanetary evolution has become a recent topic of both observational and theoretical interest [e.g. *Fan and Gibson*, 2004; *Török et al.*, 2004, 2008; *Green et al.*, 2007; *Yurchyshyn et al.*, 2007, 2009; *Lynch et al.*, 2009]. In particular, observational methods of forward modeling flux rope structures and their face-on ellipse geometry to coronagraph observations of limb and halo CMEs, respectively, has established both a reasonable link between (1) the CME source region magnetic configuration, (2) the resulting coronagraph limb or halo CME morphology, and (3) in situ measurements of the internal flux rope field structure of the associated ICME [*Thernisien*

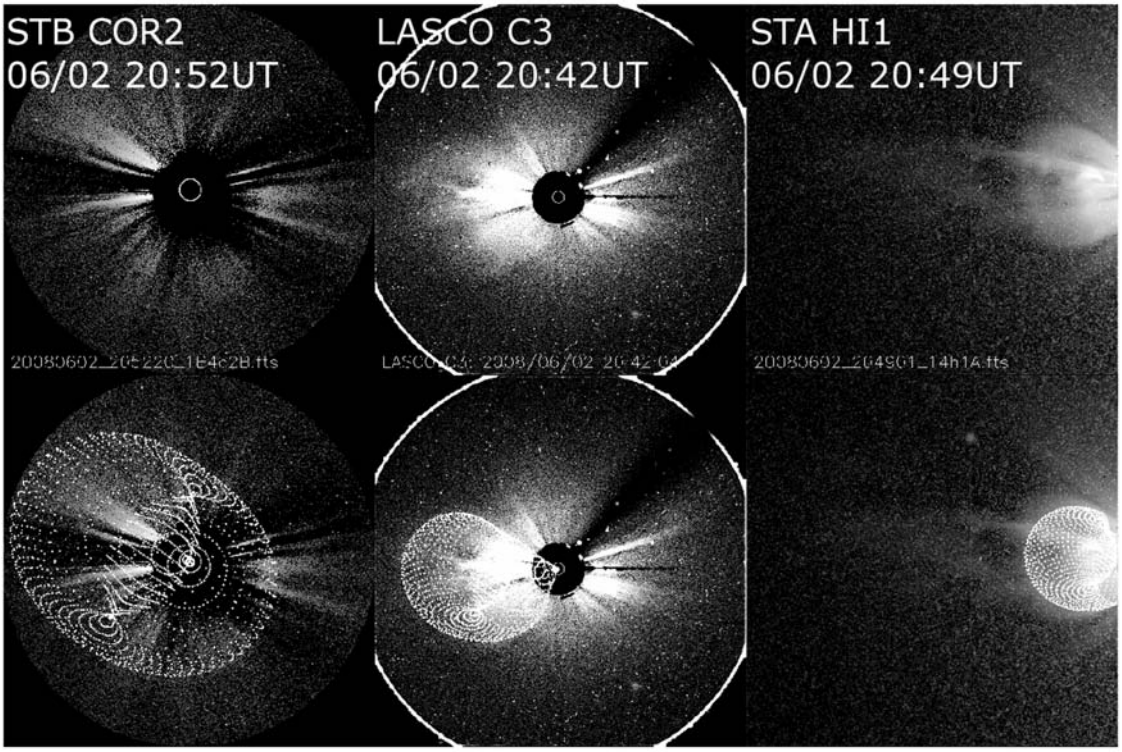

Figure 8. Representative fit of the *Thernisien et al.* [2006] forward-modeling flux rope (FR) to the imaging data. (top) A series of images corresponding to the (left) COR2-B, (middle) LASCO C3, and (right) HI1-A views of the CME at approximately 20:48 UT on 2 June 2008. (bottom) row plots the same series of images with a locus of points on the outer surface of the FR model. The rotation angle parameter defining the tilt of the FR axis with repect to the local r-ϕ plane is $\gamma = 28°$ at this time.

et al., 2006; *Krall et al.*, 2006; *Yurchyshyn*, 2008; *Yurchyshyn et al.*, 2007, 2009].

[24] Visually, the morphology of this streamer blowout CME in the running difference images tend to suggest an evolution from an initially circular flux rope with an axis orientation perpendicular to the image plane to a more elongated orientation with a significant component of the axis parallel to the image plane [e.g., see *Cremades and Bothmer*, 2004; *Thernisien et al.*, 2006; *Krall and St. Cyr*, 2006]. In the recent numerical MHD simulations of *Lynch et al.* [2009] a qualitatively similar large-scale rotation is seen for a slow magnetic breakout flux rope eruption (compare their Figure 3 to our Figures 2a–2d) where the direction of rotation is determined by the chirality/handedness of the fields.

[25] Using the forward modeling flux rope technique described by *Thernisien et al.* [2006, 2009] we have fit 67 image pairs from the STA, STB, and LASCO image sequences between 2 June 2008 01:22 UT and 3 June 2008 21:29 UT corresponding to the CME evolution through COR2, HI1, and C3 fields of view. An example of the forward modeling FR fit is shown in Figure 8 where the CME is seen in a halo configuration in COR2-B (Figure 8, left), a limb CME in HI1-A (Figure 8, right), and at an intermediate angle in LASCO C3 (Figure 8, middle). Figure 8 (top) shows the coronagraph and imaging data from the three perspectives and the bottom row overplots the locii of points on the model FR boundary for each of the above images. The magnitude of the resulting so-called rotation angle γ is plotted in Figure 9. Here, γ is defined as the angle of the model flux rope axis in the plane perpendicular to $\hat{\boldsymbol{r}}$ with $\gamma = 0°$ in the direction of $\hat{\boldsymbol{\phi}}$. The direction of the flux rope rotation during evolution is clockwise in agreement with the right-handed flux rope chirality observed by STB. The in situ STB flux rope axis orientation of $\theta_0 = 45.8°$ out of the ecliptic plane is plotted as the diamond at the event midpoint at STB as well as the horizontal dotted line. The two arrows on the x-axis represent the time of the first indication of an EUVI-A disturbance and the time the CME front becomes visible in COR2-A. The dashed line represents a linear fit to the forward modeling data implying a clockwise rotation rate of 0.68°/hr. Quantitative measurements of halo CME rotation rates by *Yurchyshyn et al.* [2009] show that this value is on the low end of their rotation rate distribution and agrees with their observation that "the bulk of slower ejecta tend to display smaller rotation rate."

[26] The forward modeling results imply a near continuous rotation through the COR2 and HI1 FOVs and we require no further rotation beyond that to match the derived in situ orientation. The estimated radial distance of the ICME at $t \sim 50$ hrs is roughly $75R_{\odot}$ or 0.35 AU. This will be an important observational constraint on the proposed models for CME/ICME rotation during initiation and propagation. It should be noted however, that the uncertainty in the forward modeling FR rotation angle parameter

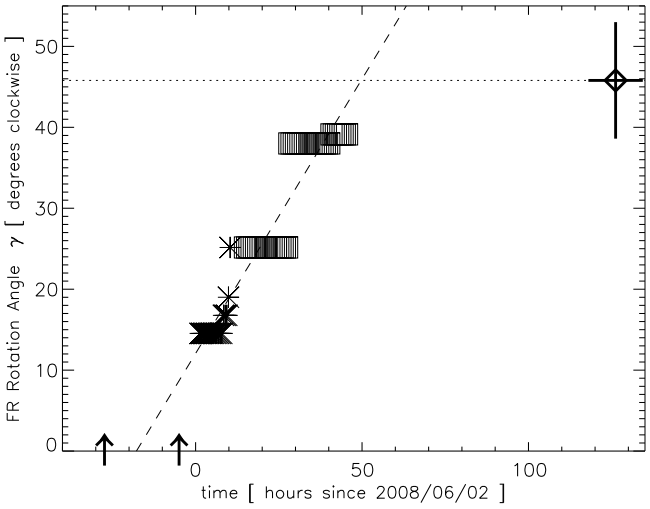

Figure 9. Evolution of the *Thernisien et al.* [2006] forward-modeling flux rope orientation. The FR model fits from COR2 (asterisks) and HI1 (squares) instruments. The in situ orientation of the STB LFF flux rope model is plotted as the diamond and dotted line at $\theta_0 = 45.8 \pm 7.2°$ with the horizontal error bar indicating the in situ event duration at STB and the vertical error bar showing the 1σ uncertainty in the fit parameter. The arrows on the time axis indicate the start of the CME event observed by EUVI-A (−27.4 hrs) and the time the CME front was visible in COR2-A (−5 hrs) from *Robbrecht et al.* [2009].

can be quite large and is probably on the order of the uncertainty in the in situ flux rope orientation parameters (which can be up to ±20° [*Lynch et al.*, 2005]). So while the actual rotation rate could be anything from 0.3°/hr to 1.0°/hr, the overall conclusion that the CME flux rope experiences some amount of slow rotation during its propagation to STB remains sound.

4.3. Angular Width and Latitudinal Expansion

[27] As we have seen in section 3, the LFF cylinder model yields a relatively good fit to the field rotation during the magnetic cloud interval. However, a single spacecraft trajectory through an ICME, even one with coherent internal field structure, yields very little information about the actual latitudinal width or angular extent of the ICME cross section. A number of studies have drawn this conclusion and a second generation of flux rope models have been developed, including non-force free elliptical cross sections [*Mulligan and Russell*, 2001] and the axisymmetric Grad-Shafranov reconstruction [*Hu and Sonnerup*, 2001]. *Riley et al.* [2004] showed that when fitting the MHD simulation of an axisymmetric flux rope propagation to 1 AU, a comparison of different methods gave similar results for small impact parameters but underestimated the cross section angular extent. *Owens* [2008] have shown, using a flux rope model with kinematic evolution [e.g., *Owens et al.*, 2006; *Owens*, 2006], that for three widely varying CME angular widths (20°, 60°, and 120°), the model's internal magnetic field profiles for a single spacecraft trajectory are virtually identical for a constant impact parameter. This motivated *Owens* [2008] to employ remote sensing coronagraph observations to attempt to constrain the CME angular width W and improve the estimate of the in situ flux content.

[28] Measuring the CME angular width in coronagraph observations that are sufficiently close to the sun to use the plane-of-sky assumption is straight forward. However, for the HI instruments using the Thomson sphere formalism we need some additional geometry to obtain the analogous angular width on planes tangent to the TS intersection with the ecliptic plane. Thus,

$$W_{\mathrm{HI1}} = \arctan\left[\frac{\tan\delta_1}{\tan\alpha_1}\right] + \arctan\left[\frac{\tan\delta_2}{\tan\alpha_2}\right], \tag{7}$$

where the coordinates $(\alpha, \delta)_i$ are the elongation and elevation angle coordinates corresponding to the upper and lower CME boundaries selected in the HI running-difference image data. The angular width measurements of the CME are plotted in Figure 10 as a function of time through the COR2 (asterisks) and HI1 (squares) instruments.

[29] The upper and lower portions of the CME signal become too faint to reliably identify during the HI2 coverage. The horizontal dotted lines indicate the instrument averages of angular width, $\langle W_{\mathrm{COR2}}\rangle = 39.7°$ and $\langle W_{\mathrm{HI1}}\rangle = 54.5°$. *Robbrecht et al.* [2009] reports an angular width for this event of 56° from the CACTus catalog [*Robbrecht and Berghmans*, 2004], in agreement with our HI1 measurements. The dashed line is a linear fit to the width measurements, yielding $dW/dt = 0.79°$/hr. However, over a decade of coronagraph observations have shown that CMEs tend to expand self-similarly, i.e. maintain a constant angular width [e.g., *St. Cyr et al.*, 2000; *Schwenn et al.*, 2005]. Given the inferred flux rope rotation from the forward modeling, the remote and in situ STEREO observations, and the theoretical support for such rotation, we expect this increase in apparent angular width is actually a line-of-sight integration

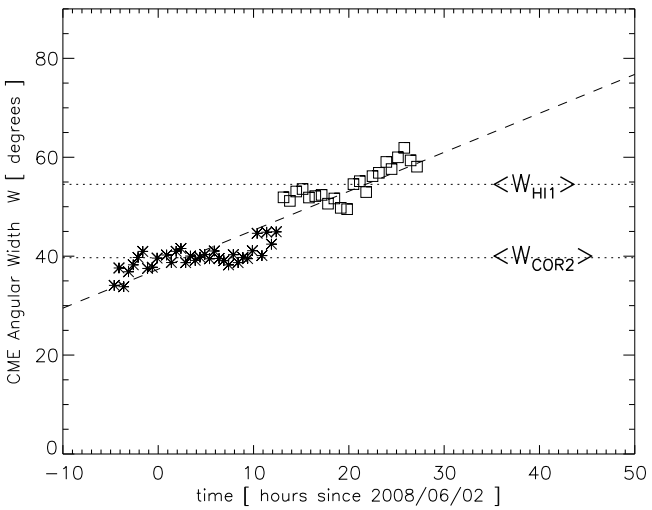

Figure 10. Evolution of the angular width of the CME measured in COR2-A (asterisks) and HI1-A (squares). The dashed line is a linear fit to the data with a slope of 0.79°/hr. The horizontal dotted lines show the average angular width in both of the instruments $\langle W_{\mathrm{COR2}}\rangle = 39.7°$ and $\langle W_{\mathrm{HI1}}\rangle = 54.5°$.

effect due to an increasing component of the flux rope axis projected onto the TS.

5. Comparing In Situ and Source Region Flux Content

5.1. In Situ ICME/MC Fluxes

[30] Magnetic flux is one of the few physical properties that can be reasonably estimated for both the CME source region and the in situ ICME/MC flux rope and therefore has become an increasingly important tool in establishing their association [e.g., see *Démoulin*, 2008, and references therein]. In practice however, establishing *quantitative* agreement between source region and in situ flux content is by no means trivial. For example, *Leamon et al.* [2002, 2004] showed that for a number of CME-ICME/MC pairs the estimated flux content from the AR source was sufficient to account for all of the observed in situ flux, however for an equal number of events the in situ flux content was greater (and sometimes much greater) than the estimated source region fluxes, leading those authors to conclude there is additional overlying helmet streamer belt flux carried out with and eventually becoming part of the eruption.

[31] *Qiu et al.* [2007] advanced this analysis by showing that a quantitative estimate of flux involved in the flare reconnection, defined by the amount of flux content swept over by the eruptive flare ribbons, can be well correlated with the in situ flux estimates, despite the uncertainties in each of these measurements. While the correlation between this measure of solar flare reconnection flux and the in situ MC flux content spanned many orders of magnitude, this approach is necessarily limited to events with well observed and defined flare ribbons, i.e. typically fast CMEs originating from active regions. We present the first comparison of the solar and in situ flux content of an event representative of the slow, streamer-blowout class of CMEs without any obvious flare ribbon signatures.

[32] Obtaining an analytical formula for the toroidal (Φ_T) and poloidal (Φ_P) magnetic flux content from the traditional constant-α LFF cylinder model is straight forward and for the section 3 fit parameters gives

$$\Phi_T^{LFF} = 0.4306\, B_0\, \pi R_c^2 = 3.01 \times 10^{20}\ \text{Mx}, \tag{8}$$

$$\Phi_P^{LFF} = 0.4152\, B_0\, L R_c = 2.98 \times 10^{21}\ \text{Mx}, \tag{9}$$

where the circular cross sectional area of the cylinder πR_c^2 appears in the expression for the axial/toroidal component and the rectangular area along the cylinder radius and along the entire cylinder "loop length", LR_c, appears in the twist/poloidal flux component [e.g., *Kumar and Rust*, 1996; *DeVore*, 2000]. For this calculation we have taken L = 2.5 AU, as from *Leamon et al.* [2004], originating from a direct observation of L by *Larson et al.* [1997]. Again, the flux estimates presented here are in excellent agreement (within 20%) to the LFF results obtained by *Möstl et al.* [2009] and in reasonable agreement with their Grad-Shafranov flux estimates (an identical poloidal flux, and within a factor of 2 of their toroidal flux).

[33] The in situ flux content has significant uncertainty associated with it– from both the difficulty in estimating L of the flux rope CME and with the underestimation of the actual cross section geometry. The true 3D ICME geometry is a much bigger source of uncertainty than the specific mathematical form of the flux rope model for the same geometry [e.g., *Dasso et al.*, 2003]. We have discussed the problems associated with measuring the flux rope/ICME angular width in situ with a single spacecraft (section 4.3) and *Mulligan and Russell* [2001] and *Owens* [2008] indicate a multiplicative factor of ~4 is required to correct the flux content obtained from the LFF model depending on the ellipticity and/or distortion of the flux rope cross section. Assuming an elliptical cross section $A^* = \pi(R_c)(r_{STB}\ \tan[0.5 W_{1AU}])$ corresponding to an angular width $W_{1AU} = \langle W_{COR2} \rangle = 39.7°$ obtained in the previous section, we can calculate a corrected axial/toroidal flux Φ_T^* from the LFF circular cross section flux as

$$\Phi_T^* = \left(\frac{A^*}{\pi R_c^2}\right)\Phi_T^{LFF} = 1.32 \times 10^{21}\ \text{Mx}, \tag{10}$$

which is $\Phi_T^* = 4.39\ \Phi_T^{LFF}$.

[34] Additionally, using the conservation of axial/toroidal magnetic flux, we can use the flux rope evolution to obtain an estimate of the coronal axial field strength associated with either the sheared filament channel, the pre-eruption coronal flux rope, or at least the CME flux rope very early in its evolution. Setting $\Phi_T^*(r_{STB}) = \Phi_T(r_{pre})$ in equation (10) for the CME near the sun using t_{pre} = 2 June 2008 00:35:40 UT corresponding to $r_{pre} = \langle V_r \rangle (t_{pre} - t_0) = 1.2 R_\odot$, $R_c(t_{pre}) = 0.0753 R_\odot$ (from equation (5)), and $W_{pre} = \langle W_{COR2} \rangle$ yields an estimate of the maximum axial field strength in the coronal flux rope of $B_0(r_{pre})$ = 6.2 G, corresponding to an average axial field component value of ~3.8 G over the flux rope's cross sectional area.

5.2. CME Source Region PFSS Fluxes

[35] We can examine the minimum energy flux content of the corona using the PFSS modeling results described in section 1 and shown in Figure 1. In fact, this is the best we can do given the complete lack of any coherent, large scale magnetic field structure at the photosphere in the vicinity of the CME source region. The left panel of Figure 11 plots the full disk MDI magnetogram on 2 June 2008 01:39 UT with the *Robbrecht et al.* [2009] source region indicated by the white box. The maximum field strengths are saturated at ±75 G and the right panel of Figure 11 plots a zoomed-in view of the source region with the field strengths saturated at ±25 G. Neither plot shows anything but typical quiet-Sun "salt and pepper" bipolar speckles. The morphology of the streamer belt in Figure 1 suggests the field that will become the toroidal/axial component of the ICME will be primarily in the ϕ-direction and the poloidal/twist component will be created out of field in the θ-direction. The amount of toroidal/axial magnetic flux in the coronal PFSS model can be calculated by

$$\Phi_T^{PFSS} = \iint B_\phi^{PFSS}(r,\theta,\phi) r dr d\theta = 2.0 \pm 0.30 \times 10^{20}\ \text{Mx}, \tag{11}$$

where we take the area integral from $1.0 R_\odot \le r \le 2.46 R_\odot$ and $-40° \le \theta \le 0°$ for several planes of constant ϕ centered

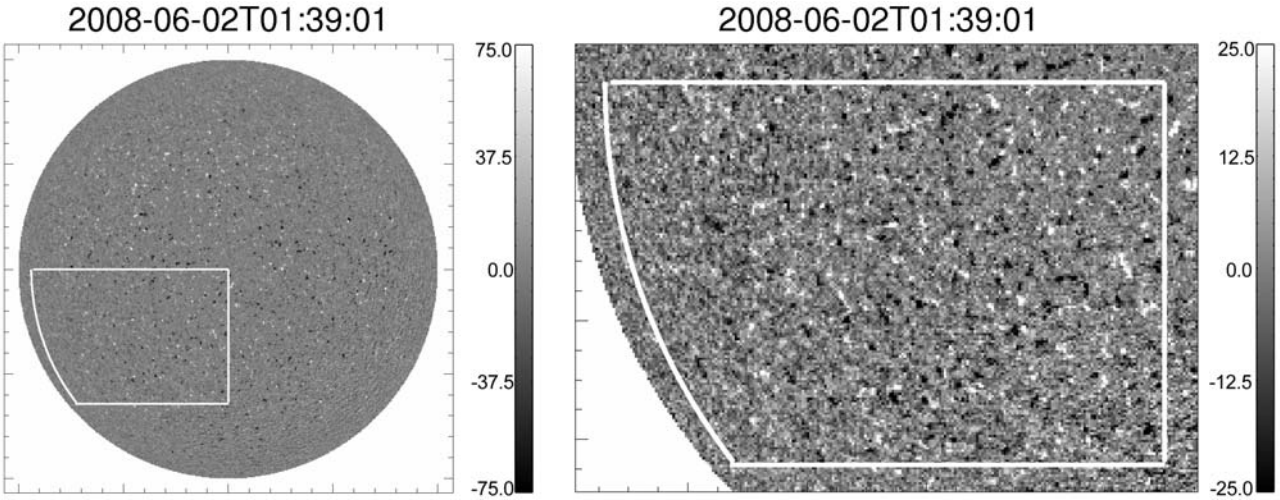

Figure 11. (left) The full disk MDI magnetogram on 2 June 2008 01:39 UT. The *Robbrecht et al.* [2009] source region is indicated by the white box covering 30° to 100° in Carrington longitude and −40° to 0° in latitude and the maximum field strengths are saturated at ±75 G. (right) A zoomed in view of the source region with the field strengths are saturated at ±25 G. The CME source region shows no large scale coherent magnetic structure.

around the longitude 64°, approximately the center of the *Robbrecht et al.* [2009] source region. Likewise, the poloidal/twist flux from the PFSS model is

$$\Phi_{\mathrm{P}}^{\mathrm{PFSS}} = \iint B_{\theta}^{\mathrm{PFSS}}(r,\theta,\phi) r \sin\theta dr d\phi = 2.0 \pm 0.14 \times 10^{21} \ \mathrm{Mx}, \tag{12}$$

where now the area integral is over r and $30° \leq \phi \leq 100°$ for several planes of constant θ centered around the latitude −20°. The value of the PFSS toroidal/axial flux is roughly a factor of 6 lower than the in situ Φ_{T}* and the value of the PFSS poloidal/twist flux is roughly a factor of 1.5 lower than the in situ $\Phi_{\mathrm{P}}^{\mathrm{LFF}}$.

[36] *Lynch et al.* [2009] recently presented an analysis of the flux evolution during MHD simulations of the initiation of slow breakout CMEs. They showed that the toroidal/axial flux stayed constant during the eruption and the poloidal flux content of the erupting flux rope increased to ~10 times the pre-eruption value. In the *Lynch et al.* [2009] simulations, the toroidal/axial flux corresponds to the highly sheared component of the pre-eruption field parallel to the polarity inversion line, whereas the poloidal/twist flux is transformed from the more potential overlying field through magnetic reconnection during the eruption. The transformation of overlying field into the poloidal/twist component of the erupting structure is common to essentially all CME models, including the loss-of-equilibrium [*Lin and Forbes*, 2000; *Roussev et al.*, 2003; *Isenberg and Forbes*, 2007], flux cancelation [*Linker et al.*, 2003; *Roussev et al.*, 2004], and breakout models [*Antiochos et al.*, 1999; *MacNeice et al.*, 2004; *Lynch et al.*, 2008]. While this is a generic feature of CME eruptions, without an estimate of the flux swept over by the flare ribbons [*Qiu et al.*, 2007], there is no way to tell just how much twist flux could be created from the overlying coronal fields. For example, in the breakout simulations by *DeVore and Antiochos* [2008] the flare reconnection added very little twist to the erupting fields. The PFSS flux estimates imply that there is plenty of poloidal flux in this portion of the helmet streamer to account for the twist flux observed in the magnetic cloud, i.e. $\Phi_{\mathrm{P}}^{\mathrm{PFSS}}$ is approximately 67% of the observed $\Phi_{\mathrm{P}}^{\mathrm{LFF}}$ value. For this particular CME, the flare reconnection is merely required to detach the energized axial or sheared component from the streamer belt into the heliosphere. However, we still require some additional energization mechanism to increase or account for the toroidal/axial or sheared flux of the pre-eruption configuration.

5.3. Large-Scale Shearing by Differential Rotation

[37] We can perform a quick back-of-the-envelope calculation to determine the feasibility of accumulating a 4–6 G field parallel to the polarity inversion line from the shearing inherent in the Sun's differential rotation. Solving the induction equation

$$\frac{\partial \boldsymbol{B}}{\partial t} = \nabla \times (\boldsymbol{v} \times \boldsymbol{B}) \tag{13}$$

for the time evolution of the magnetic field in an axisymmetric spherical coordinate system where r is the height above the coronal surface and the ϕ-coordinate is the direction of shear, we obtain

$$\frac{\partial B_{\phi}}{\partial t} = B_r \frac{\partial v_{\phi}}{\partial r} + \frac{B_{\theta}}{r} \frac{\partial v_{\phi}}{\partial \theta} - \frac{v_{\phi}}{r \sin\theta}(B_r \sin\theta + B_{\theta} \cos\theta). \tag{14}$$

It is clear that the first two terms arise from differential rotation and the third term corresponds to solid body rotation around the z-axis, i.e. $B_r \sin\theta + B_{\theta} \cos\theta$ is the field component perpendicular to $\hat{\boldsymbol{z}}$. Using the *Snodgrass* [1983] model for the differential rotation rate we find that the effective maximum shear over the *Robbrecht et al.* [2009] source region (−40° to 0° latitude) is 0.178 km/s. Estimating the magnitude of the net differential rotation shear at

V_0 = 0.20 km/s and plugging in the size of our 40° source region, $r\Delta\theta = 0.6981R_\odot$, we obtain

$$\frac{B_\phi}{\tau_s} \sim \frac{|B_r|V_0}{R_\odot} + \frac{|B_\theta|V_0}{0.70R_\odot}, \quad (15)$$

which for a characteristic field strength $|B_r| = |B_\theta| = |B|$ simplifies to $\tau_s \sim (R_\odot/2.4V_0)(B_\phi/|B|)$. To produce a shear component of B_ϕ = 4–6 G from the overall mean radial field strengths in the *Robbrecht et al.* [2009] source region where $|B|$ = 3 G, we get a differential rotation shearing timescale of $\tau_s \sim 1.9–2.9 \times 10^6$ seconds (or 22–33 days), roughly on the order of a single Carrington rotation. Here we have assumed that forming the sheared field component at or very near the solar surface is sufficient and the stressed fields are able to expand higher into the corona. Additionally, we note that differential rotation in the southern hemisphere creates right-handed sheared fields, in agreement with both the sense of rotation of the CME during its early evolution and the in situ flux rope modeling results.

5.4. Accumulation of Shear by Flux Cancelation

[38] The accumulation of a significant shear component and the resulting increase in stored magnetic energy can also be accomplished through the process of flux cancelation at the polarity inversion line [*Welsch et al.*, 2005; *Welsch*, 2006]. One way to think of the mechanism is in terms of helicity, which is approximately conserved during magnetic reconnection. This conservation implies that the annihilation of one component of flux results in an increase of the other component after reconnection such that their product, the flux linkage, or magnetic helicity, remains constant. In our source region box of length l, width $4d$, and height h, we have fluxes associated with the normal field $\Phi_r \sim \langle B_r \rangle 2dl$ and an initial shear component $\Phi_\phi \sim \langle B_\phi \rangle 4dh$. The magnetic helicity can be considered the linkage of these two flux systems $H \sim \Phi_r\Phi_\phi$ [e.g., *Moffa*, 1978]. While helicity is not precisely conserved in non-ideal processes, it is thought that the timescale for helicity decay in much longer than the magnetic diffusion timescale discussed below. Therefore, flux cancelation operating on the poloidal flux will reduce Φ_r and increase the toroidal flux Φ_ϕ such that the shear component of the field is increasingly concentrated over the polarity inversion line.

[39] If the driving flows responsible for flux cancelation are random photospheric motions [e.g., *Amari et al.*, 2003], then we can estimate a timescale for the destruction of the radial field from an effective diffusion equation,

$$\frac{\partial \boldsymbol{B}}{\partial t} = D_{\text{eff}} \nabla^2 \boldsymbol{B}. \quad (16)$$

Here, we take the diffusion coefficient to be the supergranular diffusion value $D_{\text{eff}} = 600 \pm 200$ km^2/s that is used in flux-transport models for the solar cycle evolution [*Wang et al.*, 1989] and the characteristic length scale of the diffusion region in the source box to be $d = 0.175R_\odot$ (10° either side of the polarity inversion line corresponding to half of the radial flux in our 40° source region). The timescale for the diffusive flux cancelation of B_r is then $\tau_{\text{fc}} \sim (d^2/D_{\text{eff}}) = 1.7–3.3 \times 10^7$ s (200–400 days) or approximately 7–14 Carrington rotations.

[40] This estimate suggests that shearing from differential rotation is much more effective than flux cancelation ($\tau_s \ll \tau_{\text{fc}}$), but we note that there continues to be a large discrepancy between the global flux-transport diffusion coefficient value(s) and the observed properties of individual magnetic flux elements at the photosphere. For example, *Schrijver et al.* [1997] estimate that in the quiet-Sun the flux cancelation timescale for which "as much flux cancels as is present" goes like $\tau_{\text{fc}} \sim (1.5–3)(\ell/m)$ days where ℓ/m is the ratio of collision parameters between same-polarity and opposite-polarity flux elements. If we take something like $\langle \ell/m \rangle = 3$ (i.e. one out of every 3 flux element collisions contribute to the shear component), then we might expect a timescale as short as $\tau_{\text{fc}} \sim 5–10$ days.

[41] Clearly such a wide range of flux cancelation timescales indicates further study is required to refine the quantitative estimates and resolve the apparent disconnect between the small-scale, quiet-Sun, individual flux element approach and the large-scale, flux-transport, solar dynamo approach. For our purposes here however, it is sufficient to merely present the geometric mean of each estimate as the average flux cancelation timescale of $\tau_{\text{fc}} \sim 30–60$ days (comparable to the differential rotation shearing). In general, both differential rotation and flux cancelation processes are observed to be part of the continuous evolution of the solar magnetic field and certainly each contribute to the generation and accumulation of the pre-CME sheared field.

6. Summary and Discussion

[42] The analysis presented herein is representative of the type of "whole system" approach our field is moving towards. In the first part of the paper, we summarized the propagation and evolution of the 1 June 2008 CME from the Sun to 1 AU by the STA SECCHI instruments and the associated 6 June 2008 ICME/MC observed by STB. *Möstl et al.* [2009] first presented the correspondence between the STEREO remote sensing observations and the in-situ signatures for this CME/ICME event. Here, we have independently verified a number of the *Möstl et al.* [2009] findings and have examined the heliospheric evolution of various ICME properties, including flux rope radial size, spatial orientation, and angular width. Through detailed analysis of the HI J-map we are able to show the flux rope's radial expansion is consistent with the in situ estimate of a constant V_{exp} = 24.5 km/s for the entire Sun to 1 AU journey. Using forward modeling techniques, we estimate the rotation rate of the large-scale CME flux rope at ~0.8°/hr with an overall rotation of ~45° clockwise, in agreement with recent observational and simulation results. The observed angular width provides us with a geometric correction to in situ flux rope model's circular cross section and we are able to improve the axial flux estimate derived from the LFF model.

[43] In the second part of the paper, we compared the in situ flux estimates to the fluxes contained in the PFSS model for the pre-eruption coronal fields in the CME source region. We found reasonable agreement between the poloidal/twist flux and the source region's overlying helmet streamer belt flux but had to speculate on the physical processes responsible for the generation of the pre-eruption toroidal/axial flux component. Toward this end, we pre-

sented order-of-magnitude estimates for the timescales associated with the accumulation of the necessary sheared/axial field component from both the induction equation representing the effective shear in the Sun's differential rotation and the diffusion equation representing a turbulent flux cancelation process. For this particular slow streamer-blowout CME, we conclude roughly 1–2 months of the normal, large-scale evolution of the solar magnetic field through one or both of these standard processes would be sufficient to account for the observed in situ ICME/MC fluxes. Consequently, we have a different interpretation than the *Möstl et al.* [2009] speculation that the in situ ICME flux content requires a pre-eruption highly twisted coronal flux rope. We argue that our results support the possibility that normal, everyday solar evolutionary processes are a viable source mechanism for large, gradual streamer-blowout CMEs.

[44] If these evolutionary processes were the *only* source of CME generation that operate *only* on quiet-Sun fields then we might expect 8 CMEs/month (one from each solar quadrant, frontside and backside) for a total of 96 per year. Using the 6 June 2008 magnetic cloud values as typical, these CMEs will remove on the order of $\sim 2.8 \times 10^{23}$ Mx of coronal poloidal flux and $\sim 1.2 \times 10^{23}$ Mx of coronal toroidal flux each year, which corresponds to approximately $H \sim \Phi_T \Phi_P \sim 4 \times 10^{44}$ Mx^2 of helicity shed per year and a total of 4×10^{45} Mx^2 per solar cycle. Therefore, without including any bipole emergence or source field "active region" structure, we can account for roughly 40% of the *DeVore* [2000] helicity estimate of 10^{46} Mx^2 generated by differential rotation acting on emerging bipoles and eventually removed by CMEs over the solar cycle. Likewise, our estimated rate of 8 CMEs/month is between 30–60% of the observed CME rates during the current, unusually-quiet solar minimum; according to the LASCO catalog (see http://cdaw.gsfc.nasa.gov/CME_list/), the Sun has been averaging 25.1, 13.6, and 13.5 CMEs/month (with angular widths $\geq 30°$) in 2007, 2008, and through May of 2009.

[45] It is possible, though, while such solar evolutionary processes operate continuously, their relative importance for CME generation is only significant during solar minimum when the coronal field structure is relatively stable over solar-rotation time scales. Given the interest in this particularly well observed event as a representative example of a solar minimum slow streamer-blowout CME, we encourage a coordinated community research effort to combine the remote and in situ data analysis with state of the art numerical modeling to pin down the CME initiation mechanism, benchmark our heliospheric and propagation models, and ultimately advance the field of space weather prediction and our understanding of the role CMEs play in the solar cycle.

[46] **Acknowledgments.** The authors would like to thank B. T. Welsch for helpful discussion. BJL, YL, and JGL gratefully acknowledge support from NASA HGIP NNX08AJ04G, NASA SRT NNG06GE51G, and SSL/UCB participation in the Center for Integrated Space-weather Modeling (CISM) collaboration NSF ATM-0120950. Support for the STEREO mission in situ data processing and analysis was provided through NASA contracts to the IMPACT (NAS5-03131) and PLASTIC (NAS5-00132) teams. SECCHI data used here were produced by an international consortium of the Naval Research Laboratory (USA), Lockheed Martin Solar and Astrophysics Lab (USA), NASA Goddard Space Flight Center (USA), Rutherford Appleton Laboratory (UK), University of Birmingham (UK), Max-Planck-Institut for Solar System Research (Germany), Centre Spatiale de Liége (Belgium), Institut d'Optique Théorique et Appliqueé (France), and Institut d'Astrophysique Spatiale (France). SOHO is a project of international cooperation of ESA and NASA.

[47] Philippa Browning thanks the reviewers for their assistance in evaluating this paper.

References

Amari, T., J. F. Luciani, J. J. Aly, Z. Mikić, and J. A. Linker (2003), Coronal mass ejection: Initiation, magnetic helicity, and flux ropes. I. Boundary motion-driven evolution, *Astrophys. J.*, *585*, 1073.

Antiochos, S. K., C. R. DeVore, and J. A. Klimchuk (1999), A model for solar coronal mass ejections, *Astrophys. J.*, *510*, 485.

Bothmer, V., and R. Schwenn (1994), Eruptive prominences as sources of magnetic clouds in the solar wind, *Space Sci. Rev.*, *70*, 215.

Burlaga, L. F. (1988), Magnetic clouds and force-free fields with constant alpha, *J. Geophys. Res.*, *93*, 7217.

Cremades, H., and V. Bothmer (2004), On the three-dimensional configuration of coronal mass ejections, *Astron. Astrophys*. *422*, 307.

Dasso, S., C. H. Mandrini, P. Démoulin, and C. J. Farrugia (2003), Magnetic helicity analysis of an interplanetary twisted flux tube, *J. Geophys. Res.*, *108*(A10), 1362, doi:10.1029/2003JA009942.

Davis, C. J., J. A. Davies, M. Lockwood, A. P. Rouillard, C. J. Eyles, and R. A. Harrison (2009), Stereoscopic imaging of an Earth-impacting solar coronal mass ejection: A major milestone for the STEREO mission, *Geophys. Res. Lett.*, *36*, L08102, doi:10.1029/2009GL038021.

Davies, J. A., R. A. Harrison, A. P. Rouillard, N. R. Sheeley Jr., C. H. Perry, D. Bewsher, C. J. Davis, C. J. Eyles, S. R. Crothers, and D. S. Brown (2009), A synoptic view of solar transient evolution in the inner heliosphere using the Heliospheric Imagers on STEREO, *Geophys. Res. Lett.*, *36*, L02102, doi:10.1029/2008GL036182.

Démoulin, P. (2008), A review of the quantitative links between CMEs and magnetic clouds, *Ann. Geophys.*, *26*, 3113.

DeVore, C. R. (2000), Magnetic helicity generation by solar differential rotation, *Astrophys. J.*, *539*, 944.

DeVore, C. R., and S. K. Antiochos (2008), Homologous confined filament eruptions via magnetic breakout, *Astrophys. J.*, *680*, 740.

Fan, Y., and S. E. Gibson (2004), Numerical simulations of three-dimensional coronal magnetic fields resulting from the emergence of twisted magnetic flux tubes, *Astrophys. J.*, *609*, 1123.

Farrugia, C. J., L. F. Burlaga, V. A. Osherovich, I. G. Richardson, M. P. Freeman, R. P. Lepping, and A. J. Lazarus (1993), A study of an expanding interplanetary magnetic cloud and its interaction with the Earth's magnetosphere: The interplanetary aspect, *J. Geophys. Res.*, *98*, 7621, doi:10.1029/92JA02349.

Galvin, A. B., et al. (2008), The plasma and suprathermal ion composition (PLASTIC) investigation on the STEREO observatories, *Space Sci. Rev.*, *136*, 437.

Goldstein, H. (1983), On the configuration of magnetic clouds, in *Solar Wind Five*, *NASA Conf. Publ. CP-2280*, edited by M. Neugebauer, pp. 731, NASA, Washington, D. C.

Green, L. M., B. Kliem, T. Török, L. van Driel-Gesztelyi, and G. D. R. Attrill (2007), Transient coronal sigmoids and rotating erupting flux ropes, *Solar Phys.*, *246*, 365.

Harrison, R. A., et al. (2008), First imaging of coronal mass ejections in the heliosphere viewed from outside the Sun Earth line, *Solar Phys.*, *247*, 171.

Harrison, R. A., et al. (2009), Two years of the STEREO Heliospheric Imagers (Invited review), *Solar Phys.*, *256*, 219.

Harrison, R. A., C. J. Davis, D. Bewsher, J. A. Davies, C. J. Eyles, and S. R. Crothers (2010), Coronal mass ejections in the heliospher, *Adv. Space Res.*, *45*, 1.

Howard, R. A., et al. (2008), Sun Earth Connection Coronal and Heliospheric Investigation (SECCHI), *Space Sci. Rev.*, *136*, 67.

Hu, Q., and B. U. Ö. Sonnerup (2001), Reconstruction of magnetic flux ropes in the solar wind, *Geophys. Res. Lett.*, *28*, 467, doi:10.1029/2000GL012232.

Isenberg, P. A., and T. G. Forbes (2007), A three-dimensional line-tied magnetic field model for solar eruptions, *Astrophys. J.*, *670*, 1453.

Jian, L., C. T. Russell, J. G. Luhmann, and R. M. Skoug (2006), Properties of interplanetary coronal mass ejections at one AU during 1995–2004, *Solar Phys.*, *239*, 393.

Klein, L. W., and L. F. Burlaga (1982), Interplanetary magnetic clouds at 1 AU, *J. Geophys. Res.*, *87*, 613, doi:10.1029/JA087iA02p00613.

Krall, J., and O. C. St. Cyr (2006), Flux-rope coronal mass ejection geometry and its relation to observed morphology, *Astrophys. J.*, *652*, 1740.

Krall, J., V. B. Yurchyshyn, S. Slinker, R. M. Skoug, and J. Chen (2006), Flux rope model of the 2003 October 28–30 coronal mass ejection and interplanetary coronal mass ejection, *Astrophys. J.*, *642*, 541.

Kumar, A., and D. M. Rust (1996), Interplanetary magnetic clouds, helicity conservation, and current-core flux-ropes, *J. Geophys. Res.*, *101*, 15,667, doi:10.1029/96JA00544.

Larson, D. E., et al. (1997), Tracing the topology of the October 18–20, 1995, magnetic cloud with ~0.1–10^2 keV electrons, *Geophys. Res. Lett.*, *24*, 1911, doi:10.1029/97GL01878

Leamon, R. J., R. C. Canfield, and A. A. Pevtsov (2002), Properties of magnetic clouds and geomagnetic storms associated with eruption of coronal sigmoids, *J. Geophys. Res.*, *107*(A9), 1234, doi:10.1029/2001JA000313.

Leamon, R. J., R. C. Canfield, S. L. Jones, K. Lambkin, B. J. Lundberg, and A. A. Pevtsov (2004), Helicity of magnetic clouds and their associated active regions, *J. Geophys. Res.*, *109*, A05106, doi:10.1029/2003JA010324.

Lepping, R. P., J. A. Jones, and L. F. Burlaga (1990), Magnetic field structure of interplanetary magnetic clouds at 1 AU, *J. Geophys. Res.*, *95*, 11,957.

Lin, J., and T. G. Forbes (2000), Effects of reconnection on the coronal mass ejection process, *J. Geophys. Res.*, *105*, 2375, doi:10.1029/1999JA900477.

Linker, J. A., Z. Mikić, R. Lionello, P. Riley, T. Amari, and D. Odstrcil (2003), Flux cancellation and coronal mass ejections, *Phys. Plasmas*, *10*, 1971.

Liu, Y., J. T. Hoeksema, X. Zhao, and R. M. Larson (2007), MDI synoptic charts of magnetic field: Interpolation of polar fields, *Bull. Am. Astron. Soc.*, *38*, 129.

Liu, Y., J. G. Luhmann, R. P. Lin, S. D. Bale, J. A. Davies, A. Thernisien, and A. Vourlidas (2009), Tracking CMEs/shocks and predicting their arrival time at the Earth, poster presented at NSF SHINE Workshop, Wolfville, Nova Scotia, Canada, 3–7 Aug.

Luhmann, J. G., J. T. Gosling, J. T. Hoeksema, and X. Zhao (1998), The relationship between large-scale solar magnetic field evolution and coronal mass ejections, *J. Geophys. Res.*, *103*, 6585, doi:10.1029/97JA03727.

Luhmann, J. G., et al. (2008), STEREO IMPACT investigation goals, measurements, and data products overview, *Space Sci. Rev.*, *136*, 117.

Lundquist, S. (1950), Magnetohydrostatic fields, *Ark. Fys.*, *2*, 361.

Lynch, B. J., T. H. Zurbuchen, L. A. Fisk, and S. K. Antiochos (2003), Internal structure of magnetic clouds: Plasma and composition, *J. Geophys. Res.*, *108*(A6), 1239, doi:10.1029/2002JA009591.

Lynch, B. J., J. R. Gruesbeck, T. H. Zurbuchen, and S. K. Antiochos (2005), Solar cycle-dependent helicity transport by magnetic clouds, *J. Geophys. Res.*, *110*, A08107, doi:10.1029/2005JA011137.

Lynch, B. J., S. K. Antiochos, C. R. DeVore, J. G. Luhmann, and T. H. Zurbuchen (2008), Topological evolution of a fast magnetic breakout CME in three dimensions, *Astrophys. J.*, *683*, 1192.

Lynch, B. J., S. K. Antiochos, Y. Li, J. G. Luhmann, and C. R. DeVore (2009), Rotation of coronal mass ejections during eruption, *Astrophys. J.*, *697*, 1918.

MacNeice, P. J., S. K. Antiochos, A. Phillips, D. S. Spicer, C. R. DeVore, and K. Olson (2004), A numerical study of the breakout model for CME initiation, *Astrophys. J.*, *614*, 1028.

Mierla, M., B. Inhester, C. Marqué, L. Rodriguez, S. Gissot, A. N. Zhukov, D. Berghmans, and J. Davila (2009), On 3D reconstruction of coronal mass ejections: I. Method description and application to SECCHI-COR data, *Sol. Phys.*, *259*, 123.

Moffa, H. K. (1978), *Magnetic Field Generation in Electrically Conducting Fluids*, p. 15, Cambridge Univ. Press, Cambridge, U. K.

Möstl, C., C. J. Farrugia, M. Temmer, C. Miklenic, A. M. Veronig, A. B. Galvin, M. Leitner, and H. K. Biernat (2009), Linking remote imagery of a coronal mass ejection to its in situ signatures at 1 AU, *Astrophys. J.*, *705*, L180, doi:10.1088/0004-637X/705/2/L180.

Mulligan, T., and C. T. Russell (2001), Multispacecraft modeling of the flux rope structure of interplanetary coronal mass ejections: Cylindrically symmetric versus nonsymmetric topologies, *J. Geophys. Res.*, *106*, 10,581, doi:10.1029/2000JA900170.

Owens, M. J. (2006), Magnetic cloud distortion resulting from propagation through a structured solar wind: Models and observations, *J. Geophys. Res.*, *111*, A12109, doi:10.1029/2006JA011903.

Owens, M. J. (2008), Combining remote and in situ observations of coronal mass ejections to better constrain magnetic cloud reconstruction, *J. Geophys. Res.*, *113*, A12102, doi:10.1029/2008JA013589.

Owens, M. J., P. J. Cargill, C. Pagel, G. L. Siscoe, and N. U. Crooker (2005), Characteristic magnetic field and speed properties of interplanetary coronal mass ejections and their sheath regions, *J. Geophys. Res.*, *110*, A01105, doi:10.1029/2004JA010814.

Owens, M. J., V. G. Merkin, and P. Riley (2006), A kinematically distorted flux rope model for magnetic clouds, *J. Geophys. Res.*, *111*, A03104, doi:10.1029/2005JA011460.

Qiu, J., Q. Hu, T. A. Howard, and V. B. Yurchyshyn (2007), On the magnetic flux budget in low-corona magnetic reconnection and interplanetary coronal mass ejections, *Astrophys. J.*, *659*, 758.

Riley, P., et al. (2004), Fitting flux ropes to a global MHD solution: A comparison of techniques, *J. Atmos. Sol. Terr. Phys.*, *66*, 1321.

Robbrecht, E., and D. Berghmans (2004), Automated recognition of coronal mass ejections (CMEs) in near-real-time data, *Astron. Astrophys.*, *425*, 1097.

Robbrecht, E., S. Patsourakos, and A. Vourlidas (2009), No trace left behind: STEREO observation of a coronal mass ejection without low coronal signatures, *Astrophys. J.*, *701*, 283.

Rouillard, A. P., et al. (2009), A solar storm observed from the Sun to Venus using STEREO, Venus Express, and MESSENGER spacecraft, *J. Geophys. Res.*, *114*, A07106, doi:10.1029/2008JA014034.

Roussev, I. I., T. G. Forbes, T. I. Gombosi, I. V. Sokolov, D. L. DeZeeuw, and J. Birn (2003), A three-dimensional flux rope model for coronal mass ejections based on a loss of equilibrium, *Astrophys. J.*, *588*, L45.

Roussev, I. I., I. V. Sokolov, T. G. Forbes, T. I. Gombosi, M. A. Lee, and J. I. Sakai (2004), A numerical model of a coronal mass ejection: Shock development with implications for the acceleration of GeV protons, *Astrophys. J.*, *605*, L73.

Russell, C. T., and A. A. Shinde (2003), ICME identification from solar wind ion measurements, *Sol. Phys.*, *216*, 285.

Russell, C. T., T. Mulligan, and B. J. Anderson (2003), Radial variation of magnetic flux ropes: Case studies with ACE and NEAR, in *Solar Wind Ten*, edited by M. Velli, R. Bruno, and F. Malara, *AIP Conf Proc.*, *679*, 121.

Scherrer, P. H., et al. (1995), The Solar Oscillations Investigation—Michelson Doppler Imager, *Sol. Phys*. *162*, 129.

Schrijver, C. J., A. M. Title, A. A. van Ballegooijen, H. Hagenaar, and R. A. Shine (1997), Sustaining the quiet photospheric network: The balance of flux emergence, fragmentation, merging, and cancellation, *Astrophys. J.*, *487*, 424.

Schwenn, R., A. Dal Lago, E. Huttunen, and W. D. Gonzalez (2005), The association of coronal mass ejections with their effects near the Earth, *Ann. Geophys.*, *23*, 1033.

Schwenn, R., et al. (2006), Coronal observations of CMEs, *Space Sci. Rev.*, *123*, 127.

Sheeley, N. R., Jr., J. H. Walters, Y.-M. Wang, and R. A. Howard (1999), Continuous tracking of coronal outflows: Two kinds of coronal mass ejections, *J. Geophys. Res.*, *104*, 24,739, doi:10.1029/1999JA900308.

Sheeley, N. R., Jr., et al. (2008a), SECCHI Observations of the Sun's garden-hose density spiral, *Astrophys. J.*, *674*, L109.

Sheeley, N. R., Jr., et al. (2008b), Heliospheric images of the solar wind at Earth, *Astrophys. J.*, *675*, 853.

Snodgrass, H. B. (1983), Magnetic rotation of the solar photosphere, *Astrophys. J.*, *270*, 288.

St. Cyr, O. C., et al. (2000), Properties of coronal mass ejections: SOHO LASCO observations from January 1996 to June 1998, *J. Geophys. Res.*, *105*, 18,169, doi:10.1029/1999JA000381.

Temmer, M., S. Preiss, and A. M. Veronig (2009), CME projection effects studied with STEREO/COR and SOHO/LASCO, *Sol. Phys.*, *256*, 183.

Thernisien, A. F. R., R. A. Howard, and A. Vourlidas (2006), Modeling of flux rope coronal mass ejections, *Astrophys. J.*, *652*, 763.

Thernisien, A. F. R., A. Vourlidas, and R. A. Howard (2009), Forward modeling of coronal mass ejections using STEREO/SECCHI data, *Sol. Phys.*, *256*, 111.

Török, T., B. Kliem, and V. S. Titov (2004), Ideal kink instability of a magnetic loop equilibrium, *Astron. Astrophys.*, *413*, L27.

Török, T., M. A. Berger, B. Kliem, P. Démoulin, M. Linton, and L. van Driel-Gesztelyi (2008), Twist, writhe and rotation of magnetic flux ropes in filament eruptions and coronal mass ejections, paper presented at 12th European Solar Physics Meeting, Freiburg, Germany, 8–12 Sept. (Available at http://espm.kis.uni-freiburg.de/)

Vourlidas, A., and R. A. Howard (2006), The proper treatment of coronal mass ejection brightness: A new methodology and implications for observations, *Astrophys. J.*, *642*, 1216.

Vourlidas, A., R. A. Howard, J. S. Morrill, and S. Munz (2002), Analysis of LASCO observations of streamer blowout events, in *Solar-Terrestrial Magnetic Activity and Space Environment*, *COSPAR Colloq. Ser.*, vol. 14, edited by H. Wang and R. Xu, pp. 201–208, Pergamon, Boston, Mass.

Wang, Y.-M., and N. R. Sheeley Jr. (1992), On potential field models of the solar corona, *Astrophys. J.*, *392*, 310.

Wang, Y.-M., A. G. Nash, and N. R. Sheeley Jr. (1989), Magnetic flux transport on the sun, *Science*, *245*, 712.

Webb, D. F., et al. (2009), Study of CME propagation in the inner heliosphere: SOHO LASCO, SMEI, and STEREO HI observations of the January 2007 events, *Sol. Phys.*, *256*, 239.

Welsch, B. T. (2006), Magnetic flux cancellation and coronal magnetic energy, *Astrophys. J.*, *638*, 1101.

Welsch, B. T., C. R. DeVore, and S. K. Antiochos (2005), Magnetic reconnection models of prominence formation, *Astrophys. J.*, *634*, 1395.

Yurchyshyn, V. (2008), Relationship between EIT posteruption arcades, coronal mass ejections, the coronal neutral line, and magnetic clouds, *Astrophys. J.*, *675*, L49.

Yurchyshyn, V., Q. Hu, R. P. Lepping, B. J. Lynch, and J. Krall (2007), Orientations of LASCO halo CMEs and their connection to the flux rope structure of interplanetary CMEs, *Adv. Space Res.*, *40*, 1841.

Yurchyshyn, V., V. Abramenko, and D. Tripathi (2009), Rotation of white-light coronal mass ejection structures as inferred from LASCO coronagraph, *Astrophys. J.*, *705*, 426.

Zhang, J., and K. P. Dere (2006), Statistical study of main and residual accelerations of coronal mass ejections, *Astrophys. J.*, *649*, 1100.

Zurbuchen, T. H., and I. G. Richardson (2006), In-situ solar wind and magnetic field signatures of interplanetary coronal mass ejections, *Space Sci. Rev.*, *123*, 31.

G. H. Fisher, Y. Li, J. G. Luhmann, and B. J. Lynch, Space Sciences Laboratory, University of California, 7 Gauss Way, Berkeley, CA 94720, USA. (fisher@ssl.berkeley.edu; yanli@ssl.berkeley.edu; jgluhman@ssl.berkeley.edu; blynch@ssl.berkeley.edu)

E. Robbrecht, Department of Space Physics, Royal Observatory of Belgium, Ringlaan 3, B-1180 Brussels, Belgium. (eva.robbrecht@oma.be)

A. F. R. Thernisien and A. Vourlidas, Space Sciences Division, Naval Research Laboratory, 4555 Overlook Ave. SW, Washington, DC 20375, USA. (arnaud.thernisien.ctr.fr@nrl.navy.mil; angelos.vourlidas@nrl.navy.mil)